


Brownian motion of flexibly linked colloidal ringsRuben W. Verweij ^{1,*}, Julio Melio ^{1,*}, Indrani Chakraborty ², and Daniela J. Kraft ^{1,†}¹*Huygens-Kamerlingh Onnes Laboratory, Leiden University, P.O. Box 9504, 2300 RA Leiden, The Netherlands*²*Department of Physics, Birla Institute of Technology and Science, Pilani–K K Birla Goa Campus, Zuarinagar, Goa 403726, India*

(Received 28 September 2022; accepted 4 January 2023; published 6 March 2023)

Ring, or cyclic, polymers have unique properties compared to linear polymers, due to their topologically closed structure that has no beginning or end. Experimental measurements on the conformation and diffusion of molecular ring polymers simultaneously are challenging due to their inherently small size. Here, we study an experimental model system for cyclic polymers, that consists of rings of flexibly linked micron-sized colloids with $n = 4\text{--}8$ segments. We characterize the conformations of these flexible colloidal rings and find that they are freely jointed up to steric restrictions. We measure their diffusive behavior and compare it to hydrodynamic simulations. Interestingly, flexible colloidal rings have a larger translational and rotational diffusion coefficient compared to colloidal chains. In contrast to chains, their internal deformation mode shows slower fluctuations for $n \lesssim 8$ and saturates for higher values of n . We show that constraints stemming from the ring structure cause this decrease in flexibility for small n and infer the expected scaling of the flexibility as function of ring size. Our findings could have implications for the behavior of both synthetic and biological ring polymers, as well as for the dynamic modes of floppy colloidal materials.

DOI: [10.1103/PhysRevE.107.034602](https://doi.org/10.1103/PhysRevE.107.034602)**I. INTRODUCTION**

Contrary to their well-known linear cousins, cyclic or ring polymers form a closed structure, without a beginning or an end. Their special topology imparts them with a unique set of properties different from those of linear polymers [1]. The absence of free ends suppresses reptation and results in different diffusive properties of ring polymer melts compared to melts of linear polymers [2] and the emergence of a kinetically arrested, glassy state [3]. Their cyclic nature has been proposed to induce stronger excluded volume effects on the conformational and diffusive behavior of the rings than on linear polymers [4] and can lead to a significant slowing down of polymer dynamics upon self-entanglement [5]. Understanding the impact of the topological constraint imposed by their ring-nature is also important at the single polymer level, where it might help shed light on how genomes fold themselves into volumes whose linear dimensions are many orders of magnitude smaller than their contour lengths [6]. These insights might also be used for the design of materials [7] with multifunctional and switchable properties.

To gain a better understanding of how topology induces these effects, *in situ* measurements of the diffusive dynamics and conformations of single ring polymers are needed.

*These authors contributed equally to this work.

†kraft@physics.leidenuniv.nl

Published by the American Physical Society under the terms of the [Creative Commons Attribution 4.0 International](https://creativecommons.org/licenses/by/4.0/) license. Further distribution of this work must maintain attribution to the author(s) and the published article's title, journal citation, and DOI.

Experimental measurements of their diffusive behavior have focused on ring polymers both as isolated molecules in solution [8–10] as well as in the presence of other polymers [11] and melts [12]. However, even with single-molecule techniques it is challenging to get the high spatial and temporal resolution that is required to observe both the dynamics and conformations of individual ring polymers simultaneously. For many synthetically fabricated cyclic polymers, bulk measurements are often further complicated by polydispersity in molecular weight and the presence of undesired side products stemming from the synthesis [13], with the notable exception of DNA-based ring structures. Despite these challenges, the diffusion coefficient could be obtained experimentally and was found to be larger for individual cyclic polymers in solution compared to linear polymers of similar size [8–11,14]. The scaling of the diffusion constant with molecular weight was furthermore found to not be dependent on topology for polymers in solution [9]. In contrast, a study on adsorbed polymers at an interface reports a scaling that is topology-dependent, and was attributed to the fact that the diffusion of cyclic polymers is hindered by surface asperities whereas linear polymers are not [10]. Also in the presence of other polymers, entanglement effects slow down diffusion [11]. In general, while it is clear that there is a difference between the diffusive behavior of ring and linear polymers, a direct observation of both the conformations and (short-time) diffusive behavior is lacking.

To circumvent this limitation, we here use flexible rings made of colloidal particles as model systems instead. Because of their unique combination of microscopic size and their sensitivity to thermal fluctuations [15–17], their diffusive properties can be directly studied using well-established techniques, such as optical microscopy, that provide full

information of their conformation with high time resolution. Indeed, for reconfigurable colloidal rings built from patchy particles bound via critical Casimir interactions, it was found recently that colloidal analogues of cyclopentane show similar conformational transformations as their atomic counterparts [18]. Due to their limited reconfigurability, however, they are unsuitable to serve as analogues for ring polymers. In contrast, flexible structures built from spherical colloid-supported lipid bilayers (CSLBs) [19,20] were found to be completely freely jointed up to steric exclusions [21,22]. While the experimentally achievable maximum length is limited to a few repeating units, precluding a study of effects such as self-entanglement and knotting, their slower dynamics and quasi-2D confinement compared to real molecules make them excellent model systems to study their diffusive properties and conformations *in situ*.

In this work, we study experimentally and numerically a model system of micron-sized colloidal rings, built from CSLBs, to obtain a detailed understanding of the conformational and diffusive properties of flexible rings. We consider rings of four to eight spherical particles and study both their conformations and diffusive behavior. The experimentally feasible size range implies that secondary structural effects commonly observed for longer polymers, such as knotting or supercoiling, are geometrically forbidden. We find that while the smaller rings show no preferred conformations, preferences arise for the larger rings, because of the increase in degrees of freedom in combination with steric constraints, stemming from the fact that the particles cannot interpenetrate. Both the translational and rotational diffusivity of the rings is greater than that of chains of the same size, because of their smaller radius of gyration. Interestingly, their flexibility, which characterizes the rate of mean-squared conformational changes, is lower than that of chains. We show that constraints stemming from the ring structure cause this decrease in flexibility and infer the expected scaling of the flexibility as function of ring size. Our findings may have implications for the behavior of both synthetic and biological ring polymers, as well as for the dynamic modes of floppy colloidal materials.

II. MATERIALS AND METHODS

A. Experimental

Flexible colloidal rings were assembled from colloid-supported lipid bilayers (CSLBs) [19,20]. We followed the preparation protocol for the CSLBs as described by Ref. [21]. We employed $2.12 \pm 0.06 \mu\text{m}$ silica particles as supports, that were coated with a fluid lipid bilayer by deposition and rupture of small unilamellar vesicles consisting of 98.8 mol% of the phospholipid DOPC [(Δ 9-Cis) 1,2-dioleoyl-sn-glycero-3-phosphocholine], 1 mol% of the lipopolymer DOPE-PEG(2000) [1,2-dioleoyl-sn-glycero-3-phosphoethanolamine-N-[methoxy(polyethylene glycol)-2000]] and 0.2 mol% of the fluorescently labeled TopFluor-Cholesterol [3-(dipyrrometheneboron difluoride)-24-norcholesterol] or, alternatively, the same amount of the fluorescently labeled DOPE-Rhodamine [1,2-dioleoyl-sn-glycero-3-phosphoethanolamine-N-(lissamine rhodamine B sulfonyl)]. Bilayer coating was performed in a buffer

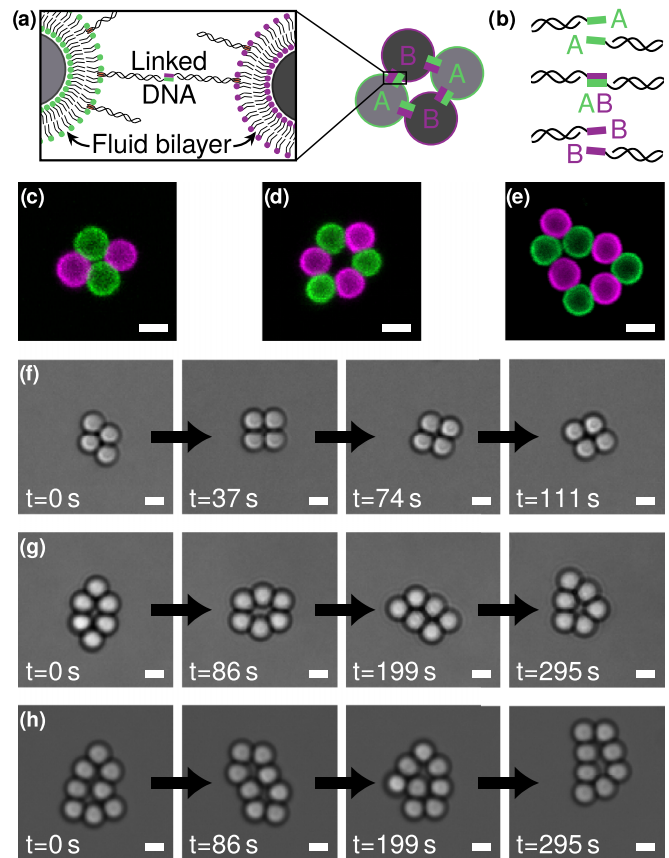


FIG. 1. Flexibly linked colloidal loops. (a) The flexible rings are built from colloid-supported lipid bilayers (CSLBs). CSLBs consist of spherical silica colloids coated with a fluid lipid bilayer. DNA linkers are inserted into the bilayer using a hydrophobic anchor. Because of the fluid lipid bilayer, the linkers can diffuse on the surface of the particles and therefore, the particles can move with respect to each other whilst staying bonded. (b) The DNA linkers are functionalized with sticky ends A that are complementary to sticky ends B, so that particles functionalized with A-type linkers can only form bonds with particles coated with B-type linkers. [(c)–(e)] Confocal images of a tetramer (c, $n = 4$), hexamer (d, $n = 6$), and octamer (e, $n = 8$) loop. (f–h) Bright field snapshots of a flexible tetramer (f, $n = 4$), hexamer (g, $n = 6$), and octamer (h, $n = 8$) ring, which show shape changes that are more pronounced for the larger rings. Scale bars in panels [(c)–(h)] are $2 \mu\text{m}$.

at pH 7.4 containing 50 mM sodium chloride (NaCl) and 10 mM [4-(2-Hydroxyethyl)-1-piperazineethanesulfonic acid (HEPES)]. We added double-stranded DNA (of, respectively, strands DS-H-A and DS-H-B, see the Supplemental Material of Ref. [21]) with an 11 base pair long sticky end and a double stearyl anchor, which inserts itself into the bilayer via hydrophobic interactions, as shown Fig. 1(a). The sticky end of strand DS-H-A is complementary to the sticky end of strand DS-H-B, which allows them to act as linkers. DNA hybridization and experiments were performed in a different buffer of pH 7.4, containing 200 mM NaCl and 10 mM HEPES. Rings of $2.12 \mu\text{m}$ CSLBs were formed by self-assembly or via manual assembly using optical tweezers, in a sample holder made of polyacrylamide (PAA)-coated cover glass [21]. Confocal microscopy images of the coated

TABLE I. Overview of the number of measurements, the total duration, and the total number of frames per ring size, for the experimental and simulated data.

n	Measurements		Duration [min]		Total frames	
	Expt.	Sim.	Expt.	Sim.	Expt.	Sim.
4	14	20	196	600	2.2e5	2.5e7
5		20		600		2.5e7
6	10	20	141	600	1.7e5	2.5e7
7		20		600		2.5e7
8	9	20	110	600	1.3e5	2.5e7

particles are shown in Fig. 1(c) for a tetramer loop, Fig. 1(d) for a hexamer loop and Fig. 1(e) for an octamer loop.

B. Microscopy

Loops were imaged for at least 5 min (frame rates between 5 and 20 fps) at room temperature using an inverted confocal microscope (Nikon Eclipse Ti-E) equipped with a Nikon A1R confocal scanhead with galvano and resonant scanning mirrors. A $60\times$ water immersion objective (NA = 1.2) was used. Lasers of 488 and 561 nm were used to excite, respectively, the TopFluor and Rhodamine dyes. Laser emission passed through a quarter wave plate to avoid polarization of the dyes and the emitted light was separated by using 500–550 nm and 565–625 nm filters.

To complement the data obtained from self-assembled loops, we used optical tweezers to assemble specific cluster sizes. For the hexamer and octamer loops, the probability of forming such a loop using the self-assembly method we used here is low, therefore these were formed exclusively using optical tweezers. Briefly, we employed a homemade optical setup consisting of a highly focused trapping laser manufactured by Laser QUANTUM (1064 nm wavelength). The laser beam entered the confocal microscope through the fluorescent port, after first passing through a beam expander and a near-infrared shortpass filter. The same objective was used for imaging and to focus the trapping laser beam. During the trapping, the quarter wave plate was removed from the light path.

Particle positions were tracked using a custom algorithm [20] available in TrackPy by using the `locate_brightfield_ring` function [23] or using a least-square fit of a Mie scattering based model implemented in HoloPy [24]. Both methods agree to an accuracy of at least 1 px; however, we have found that the Mie scattering based model is more robust for tracking multiple particles in close proximity to each other. For all analysis, we only selected rings that showed all bond angles during the measurement time, experienced no drift and were not stuck to the substrate. An overview of the total number of measurements, the total duration and the total number of frames per ring size is shown in Table I.

C. Simulations

We have performed Brownian dynamics simulations with hydrodynamic interactions following the method outlined

in Sprinkle *et al.* [25] using the open-source RigidMulti-blobsWall package [26]. The procedure is identical to the method described in Verweij *et al.* [22], which we now briefly summarize. Hydrodynamic interactions are calculated using the Stokes equations with no-slip boundary conditions. The hydrodynamic mobility matrix is approximated using the Rotne-Prager-Blake (RPB) tensor [27], which is a modified form of the Rotne-Prager-Yamakawa (RPY) tensor [28–30] and accounts for a bottom wall, which is unbounded in the transverse directions. These corrections to the RPY tensor are combined with the overlap corrections described in Wajnryb *et al.* [30] to prevent particle-particle and particle-wall overlap. The RPB mobility inaccurately describes near-field hydrodynamic interactions and therefore breaks down for small separation distances. This can be overcome by adding a local pairwise lubrication correction to the RPB resistance matrix as described in detail in Sprinkle *et al.* [25]. Based on the full lubrication-corrected hydrodynamic mobility matrix, the Ito overdamped Langevin equation is solved to describe the effect of thermal fluctuations.

We include a gravitational force on the particles to confine them to diffuse close to the bottom wall, as in the experiments. Interparticle bonds are modeled by harmonic springs of stiffness $1000 k_B T / R^2$ and equilibrium length $2R$, where $R = 1.06 \mu\text{m}$ is the particle radius. The bond angle is not restricted. We set the temperature $T = 298 \text{ K}$, the viscosity of the fluid $\eta = 8.9 \times 10^{-4} \text{ Pa s}$, the gravitational acceleration $g = 9.81 \text{ m s}^{-2}$, the particle mass $m_p = 9.5 \times 10^{-15} \text{ kg}$ (by assuming a particle density of 1900 kg m^{-3}) and the simulation timestep $\Delta t = 1.42 \text{ ms}$. For the firm potential that prevents overlap, we use a strength of $4k_B T$ and a cutoff distance [25,31] $\delta_{\text{cut}} = 10^{-2} R$. We initialized the particle loops in the configuration given by the regular polygon of the same size. Then, these initial configurations were randomized by running the integration for a simulated time of 60 s prior to saving the configurations, to ensure a proper equilibration of the particle positions, bond lengths, velocities and opening angles. The particle positions were saved every 8 simulation steps to obtain a final framerate of approximately 90 fps. An overview of the total number of simulations, the total duration and the total number of saved frames per loop size is shown in Table I.

For comparison to the simulated and experimental data, we have generated permutation data, in which the rings are completely noninteracting and freely jointed up to steric exclusions. First, we have generated all permutations of the $(n - 3)$ independent opening angles θ_i , each of which can take on $N_\theta = (360 - 2 \times 60) / (\delta\theta)$ different values, where $\delta\theta$ denotes the bin width. The opening angles are indicated by the blue arcs in the schematics of Fig. 2 for all ring sizes. This gives a total number of $P(N_\theta, n - 3) = N_\theta! / (N_\theta - (n - 3))!$ combinations of the $(n - 3)$ opening angles θ_i . Second, we removed those combinations that are forbidden because of steric exclusions between particles. After removing these configurations, we checked if the topology of the structure was correct and removed configurations of the wrong topology, i.e., structures that did not form a closed ring. This resulted in the final allowed combinations, which we call “permutation data”.

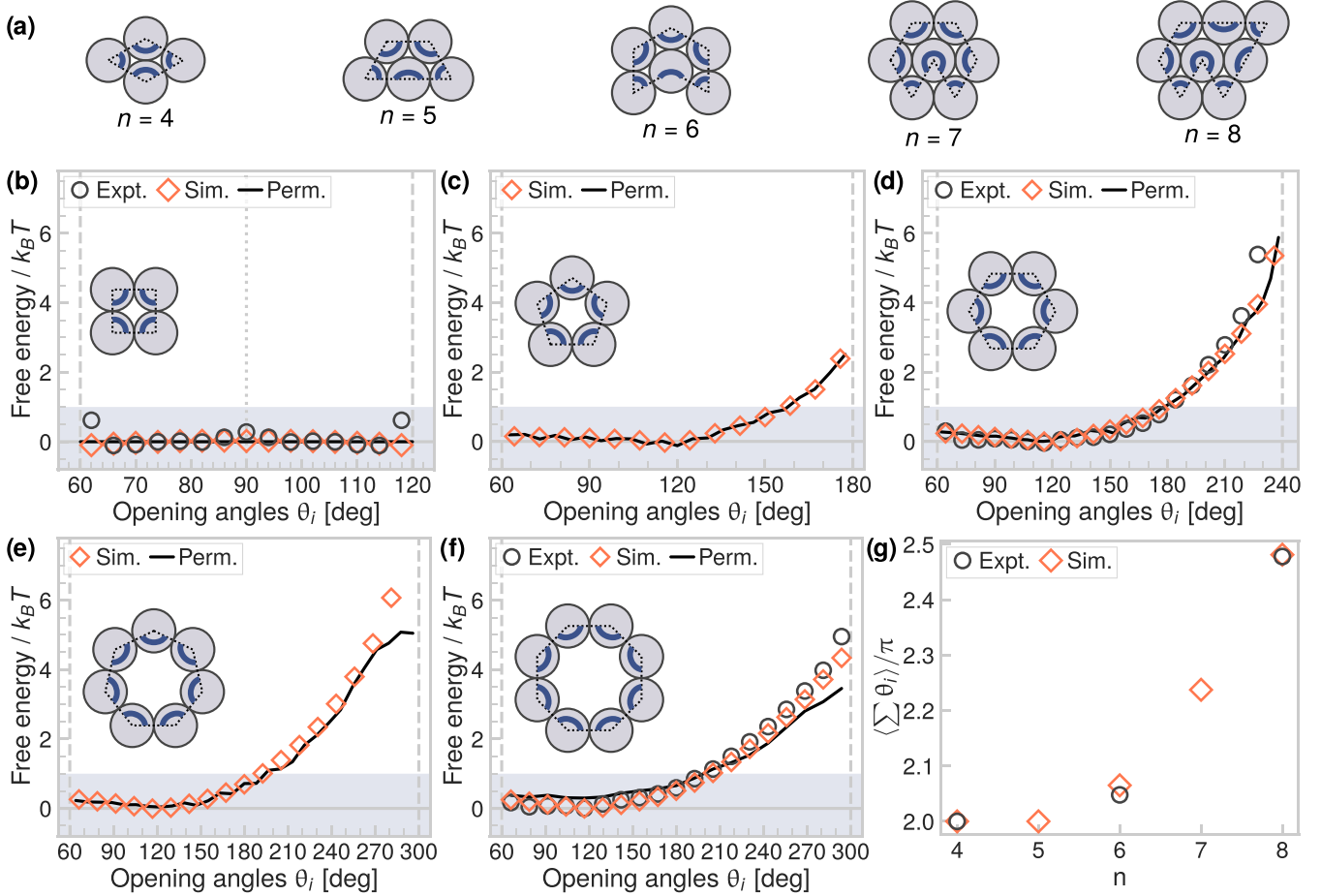


FIG. 2. Conformations of flexibly linked colloidal loops. (a) The most compact configurations for all rings studied here, from $n = 4$ – 8 . The opening angles θ_i are indicated by the blue arcs. [(b)–(f)] The free energy of (b) tetramer ($n = 4$), (c) pentamer ($n = 5$), (d) hexamer ($n = 6$), (e) heptamer ($n = 7$), and (f) octamer ($n = 8$) rings, for \circ experimental, \diamond simulated, and permutation data (black line). The shaded area indicates free energy differences lower than the thermal energy. Blue lines indicate internal opening angles taken into account. The free energy was determined using Boltzmann weighing of the joint probability density function of all opening angles θ_i . (g) Mean total curvature of the loops as function of n for the experimental and simulated data.

D. Diffusion tensor analysis

1. The definition of the coordinate system

As tracking point, we have used the center of mass (c.m.), which is the same as the center of diffusion (c.d.) for our colloidal rings. The tracking point should be carefully considered, because it affects the magnitude of the diffusion tensor [32,33]. The c.d. yields the lowest value of the diffusion tensor [33]. The coordinate system used here is identical to the coordinate system described in Verweij *et al.* [22] and we briefly summarize its definition here. The direction of the body-centered x and y axes was determined as function of the tracking point $\mathbf{r}_{\text{t.p.}}$, which defines the origin of the body-centered coordinate frame. We define

$$\mathbf{r}_{\text{t.p.}} = \rho_1 \mathbf{r}_1 + \rho_2 \mathbf{r}_2 + \cdots + \rho_n \mathbf{r}_n, \quad (1)$$

which defines the location of the tracking point as a linear combination of the particle positions [33]. $\boldsymbol{\rho} = (\rho_1, \rho_2, \dots, \rho_n)$ is a weight vector which determines how much weight is accorded to each particle in the calculation of the tracking point $\mathbf{r}_{\text{t.p.}}$. As an example, for a tetramer ring, $\boldsymbol{\rho} = (1/n = 1/4, 1/4, 1/4, 1/4)$.

The direction of the x axis was chosen as

$$\hat{\mathbf{x}} = \pm \left[\frac{\mathbf{r}_{\text{t.p.,}1} + \cdots + \mathbf{r}_{\text{t.p.,}s_1}}{\rho_1 + \cdots + \rho_{s_1}} - \frac{\mathbf{r}_{\text{t.p.,}s_2} + \cdots + \mathbf{r}_{\text{t.p.,}n}}{\rho_{s_2} + \cdots + \rho_n} \right], \quad (2)$$

where $\mathbf{r}_{\text{t.p.,}i}$ is the i th coordinate of the tracking point and the loop is split into two parts with equal numbers of particles according to

$$\begin{aligned} s_1 = s_2 = \left\lceil \frac{n}{2} \right\rceil & \quad \text{for odd } n, \\ s_1 = \left\lceil \frac{n}{2} \right\rceil, s_2 = s_1 + 1 & \quad \text{for even } n. \end{aligned} \quad (3)$$

$\hat{\mathbf{y}}$ is then chosen such that $\hat{\mathbf{x}}$ and $\hat{\mathbf{y}}$ form a right-handed coordinate system, where the direction of $\hat{\mathbf{y}}$ is chosen to point along $\mathbf{r}_{\text{t.p.}} - (\mathbf{r}_{s_1} + \mathbf{r}_{s_2})/2$. This orientation was determined for every frame, which fixed the orientation of the body-centered coordinate system $\mathbf{x}(\tau = 0), \mathbf{y}(\tau = 0)$. For subsequent lag times, the direction of $\mathbf{y}(\tau)$ was chosen such that $\mathbf{y}(\tau = 0) \cdot \mathbf{y}(\tau) > 0$, i.e., the direction of \mathbf{y} does not change sign. The resulting coordinate system relative to the c.d. is visualized for the tetramer loops in Fig. 4(a).

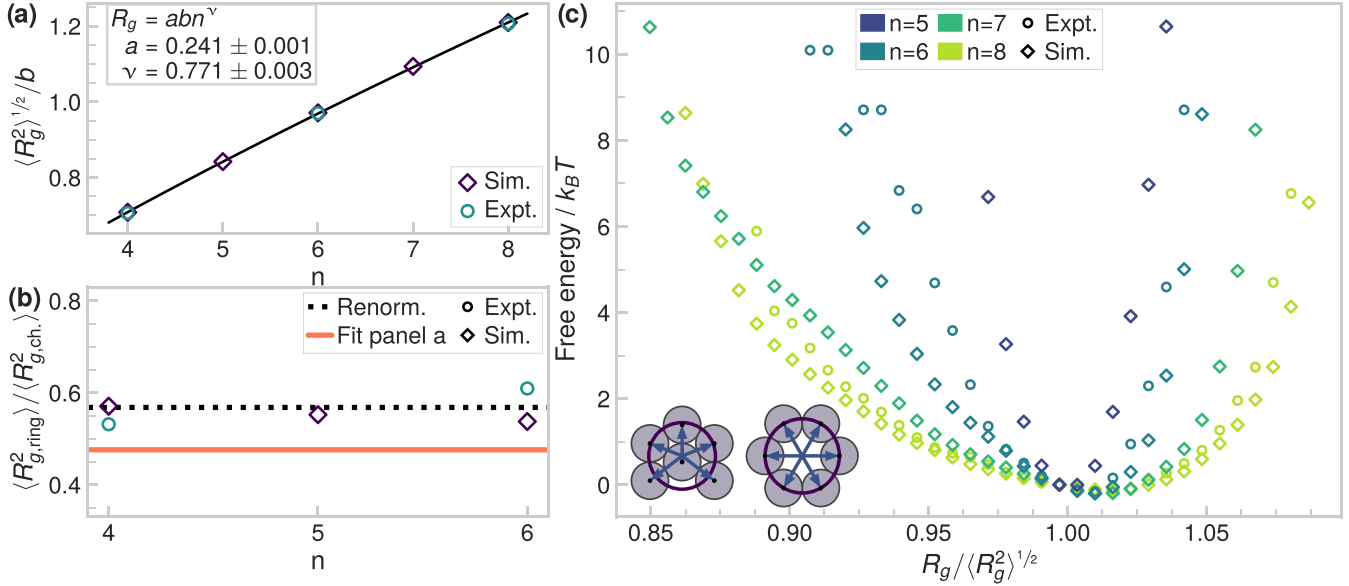


FIG. 3. Radius of gyration of colloidal rings. (a) The radius of gyration in units of the bond length b scales as function of n as predicted by Eq. (9), which is also shown in the inset, along with the values of the fitted parameters. (b) The ratio between the radius of gyration of rings and chains is close to the value predicted by renormalization theory [4,37], as shown for the experimental and simulated data that are available for both the rings and chains. Additionally, the solid line indicates the ratio of the scaling found in panel a for rings and the previously determined scaling of chains, which takes into account all available ring ($n = 4$ to 8) and chain ($n = 3$ to 6) lengths. (c) The free energy in terms of the radius of gyration divided by its average value for all ring sizes. The distribution is asymmetric and covers a wider range of possible values for the larger ring sizes. Note that the radius of gyration of tetramer rings is constant and therefore not included here. The schematics show a circle with its radius equal to the radius of gyration of the most compact (left) and most extended (right) hexamer ring.

2. Definition of the diffusion tensor

We have determined the short-time diffusivity of the rings, both as function of their instantaneous shape for the tetramer rings, as well as averaged over all possible configurations for all loop sizes. Because the rings are sedimented to the bottom substrate, we consider only the quasi-2D, in-plane diffusivity.

For all rings, we have determined the short-time diffusion tensor,

$$D[ij] \equiv \frac{1}{2n} \frac{\partial \langle \Delta i \Delta j \rangle_\tau}{\partial \tau}, \quad (4)$$

with τ the lag time between frames, $\langle \dots \rangle_\tau$ denotes a time average over all pairs of frames a lag time τ apart and $\Delta i = i(t + \tau) - i(t)$ is the displacement of the i th diffusion tensor element. The average diffusion tensor elements $D[ij]$ were obtained by fitting the overall slope of the mean-squared displacements as a function of lag time τ . We considered lag times up to 0.25 s for all experiments, set by the slowest frame rate of the experimental data. In simulations, lag times up to 0.05 s were considered. For fitting the slopes of the MSDs, we used a standard least-square fit of a linear model with an intercept, to characterize the localization error [34].

Using Eq. (4), we have calculated the shape-averaged, quasi-2D translational diffusion coefficient corresponding to in-plane diffusivity above the wall and given by $D_T = D[\mathbf{r}_{t.p.}, \mathbf{r}_{t.p.}]$, where $\mathbf{r}_{t.p.}$ is the position of the loop relative to the tracking point defined by Eq. (1). Additionally, we determined the rotational diffusion coefficient $D[\alpha\alpha]$ from the mean-squared angular displacement of the x axis [defined in Eq. (2), as depicted schematically in Fig. 4(a) for the tetramer loop], which describes the rotational diffusivity around an axis

perpendicular to the substrate. Finally, we determine the overall cluster flexibility $D[\theta\theta]$ by calculating the mean-squared displacements of all n opening angles θ_i as follows:

$$\langle |\Delta\theta|^2 \rangle_\tau = \langle |(\Delta\theta_1, \dots, \Delta\theta_n)|^2 \rangle_\tau. \quad (5)$$

Here, $\langle \dots \rangle_\tau$ denotes a time average over all pairs of frames a lag time τ apart and $\Delta\theta_i = \theta_i(t + \tau) - \theta_i(t)$ is the displacement of the i th opening angle θ . Finally, the flexibility $D[\theta\theta]$ is given by

$$\langle |\Delta\theta|^2 \rangle_\tau = 2nD[\theta\theta]\tau, \quad (6)$$

analogously to the other diffusion tensor elements.

3. Shape-dependent diffusivity of the tetramer loops

For the flexible tetramer loops, in addition to the *shape-averaged* short-time diffusion tensor, we have calculated the *shape-dependent* short-time diffusion tensor. This is feasible for the tetramer loop because its shape is fully characterized by using only one opening angle. To do so, we have calculated a 4×4 diffusion tensor, where the four degrees of freedom correspond to translational diffusivity in x and y , rotational diffusivity and the flexibility of the tetramer loop, which is described by the diffusivity of the opening angles θ_i , which we have defined in Eq. (6). Specifically, for the tetramer loop, the x and y directions are schematically shown for one configuration in Fig. 4(a) and defined by Eq. (2). The rotation angle used for determining the rotational diffusivity is indicated in Fig. 4(a) and is the angle of the $x(\tau)$ relative to $x(\tau = 0)$, i.e., the angle of the body-centered x axis of the current frame relative to the body-centered x axis of the reference frame

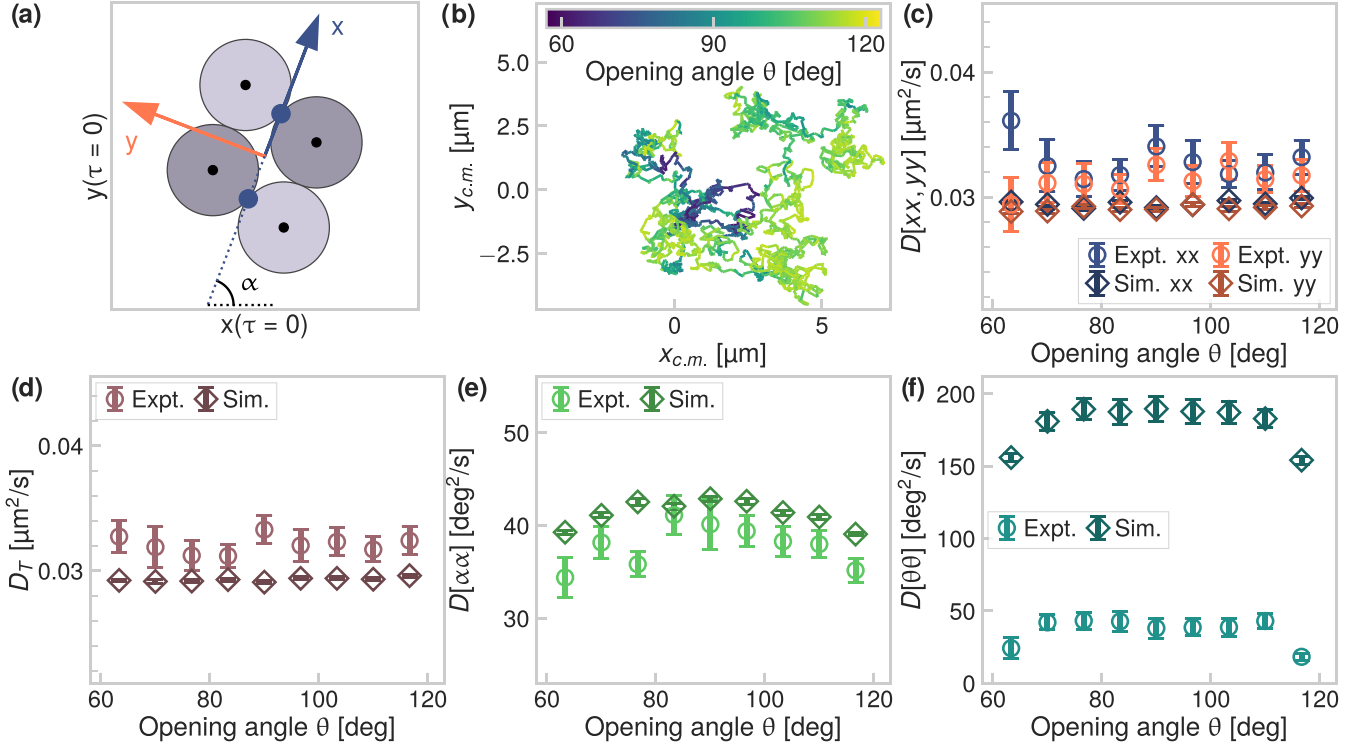


FIG. 4. Diffusion of flexible tetramer loops. (a) An illustration of the coordinate system used to analyze the diffusivity of the tetramer rings, as defined in Sec. IID. (b) The displacement of the center of mass (c.m.) of a 10 min experimental measurement of a tetramer loop. The color indicates the instantaneous value of one of the opening angles θ . [(c)–(f)] We have compared the diffusion tensor elements calculated from \diamond simulated and \circ experimental data. (c) The translational diffusion along the x and y directions is comparable in magnitude and shows little shape dependence. (d) The in-plane translational diffusion coefficient D_T . We find that $\langle D_{\text{expt}}/D_{\text{sim}} \rangle = 1.10 \pm 0.02$. (e) The rotational diffusivity, for which $\langle D_{\text{expt}}/D_{\text{sim}} \rangle = 0.92 \pm 0.04$. (f) Compared to the simulated flexibility, the experimental flexibility is much lower, namely $\langle D_{\text{expt}}/D_{\text{sim}} \rangle = 0.20 \pm 0.04$. All off-diagonal diffusion tensor elements are close to zero.

at $\tau = 0$. The flexibility is calculated from the mean-squared displacement of the opening angle θ . As illustrated by the blue arcs in the schematic of Fig. 2(b), θ is defined in such a way that it is always less than or equal to 120 deg.

The diffusion tensor elements of the tetramer loops were determined analogously to the trimers [21]. Briefly, for each pair of frames, we determined the initial shape of the ring, which is characterized by the opening angle θ . We only considered trajectories where the variation in θ did not exceed the edges of the bin describing the initial shape. That is, we divided the possible values of θ in bins and calculated the short-time diffusivity given by Eq. (4) for all combinations of lag times where $\theta(\tau)$ remained in the same bin as $\theta(0)$, which were then stored according to their respective θ -bins. In that way, we calculated the diffusion tensor elements separately for each initial shape.

III. RESULTS AND DISCUSSION

A. Free energy of different conformations of flexible loops

We designed our colloidal model system for ring polymers by assembling flexible rings of colloid-supported lipid bilayers (CSLBs), i.e., colloidal silica particles surrounded by a fluid lipid bilayer [19,20]. We equip the CSLBs with strong and specific bonds imparted by DNA linkers with single stranded sticky ends that are inserted into the lipid bilayer.

The DNA linkers are mobile on the CSLB surface allowing for configurational flexibility of structures assembled from bonded CSLBs also after assembly [21,22,35]. We employed two types of DNA linkers with complementary sticky ends, which we label A and B, such that A only binds to B and not to itself; see Fig. 1(b). The colloidal size of our model system allows us to observe the position of the constituent spheres using bright field microscopy. We visualize their functionalization with the two strands as well as their correct and selective binding by integrating dyes with the DNA linkers, and imaging the rings with confocal microscopy; see Figs. 1(c)–1(e). The use of two complementary sticky ends A and B reduces, or, in the case of a tetramer loop, even prevents adhesion between opposing particles in the ring and hence a change of its topology and reconfigurability. This strategy limits our experiments to even-numbered ring sizes, of which we assembled tetramers ($n = 4$), hexamers ($n = 6$), and octamers ($n = 8$). We therefore compared and complemented our experiments with Brownian dynamics simulations for colloidal rings with $n = 4 - 8$ constituent spheres. In these simulations, hydrodynamic interactions between particles and the substrate were taken into account via the Rotne-Prager-Blake (RPB) tensor [27], overlap corrections [30] and a local pairwise lubrication correction [25] (see Sec. II C for details).

The thus assembled colloidal rings show constant shape changes induced by thermal fluctuations. The full flexibility

of the rings is clearly visible in the representative time series from bright field microscopy movies of flexible tetramers, hexamers, and octamers; see Figs. 1(f)–1(h) and corresponding movies in the Supplemental Material [36]. Tetramers possess only one internal degree of freedom and randomly transitions between diamond-like configurations with internal opening angles θ_i between $60 \text{ deg} \leq \theta_i \leq 120 \text{ deg}$. With increasing ring size, the number of degrees of freedom rises and the constrained motion observed in the tetramer is gradually lifted. Hexamers and octamers possess three and five internal degrees of freedom, respectively, and can adopt an increasingly wider range of shapes. Correspondingly, the maximum internal opening angle that is geometrically possible increases from 180 deg for $n = 5$, to 240 deg for $n = 6$ and to 300 deg for $n \geq 7$, the maximum that is achievable for three otherwise unconstrained particles in a chain [see Fig. 2(a)]. At $n = 7$ a compact hexagonal structure is required for attaining this maximum internal angle. Additional particles beyond $n = 7$ in the ring do not increase the maximum internal opening angle, but the number of conformations of the remaining particles in case that any three take on the maximum internal angle is higher. In turn, this increases the probability to observe a configuration with the maximum value of the opening angle.

To quantify the conformations of the colloidal rings, we measured all n indistinguishable internal opening angles θ of a ring of size n and calculated the probability density function $p(\theta)$. From this, we determined the free energy F using Boltzmann weighing,

$$\frac{F}{k_B T} = -\ln p(\theta) + \frac{F_0}{k_B T}, \quad (7)$$

where k_B is the Boltzmann constant, T the temperature, and F_0 is a constant and arbitrary offset to the free energy. The probability density function $p(\theta)$ is calculated from the histogram of all observed angles for rings of a given size, by dividing the number of observed angles in a given angular bin by the bin width and the total number of observations. The angular range is determined purely by geometry: the minimum opening angle is $\theta = 60 \text{ deg}$ and the maximum angle depends on n and is limited by the constraints induced by the topology and geometry, as shown in Fig. 2(a) and ranges from $\theta = 120 \text{ deg}$ for $n = 4$ to $\theta = 300 \text{ deg}$ for $n \geq 7$ as noted before.

We plot the obtained values for the free energy as a function of the possible range of opening angles for rings of $n = 4$ –8 in Fig. 2. For all datasets, we set the free energy to 0 at the smallest value and compare it to the thermal energy of $1 k_B T$, which is indicated by the shaded area. The tetramer rings show no preference for any opening angle with respect to the thermal energy. They transition freely and with equal probability between all possible internal opening angles, as shown in Fig. 2(b). For the pentamer loops, however, the free energy exceeds the thermal energy for large internal opening angles $\theta_i \geq 158 \text{ deg}$; see Fig. 2(c). Similarly, for $n = 6$ –8 we also find that the free energy exceeds the thermal energy for increasingly greater values of the opening angles: for hexamer loops this occurs if $\theta_i \geq 178 \text{ deg}$, for heptamer loops if $\theta_i \geq 192 \text{ deg}$, and for octamer loops if $\theta_i \geq 204 \text{ deg}$. This finding implies that smaller opening angles occur more frequently, leading to an effective free energy preference, and is found both in experimental measurements and simulations.

We can attribute this free energy preference to the steric constraints imposed by the ring topology and self-avoidance of the segments of the ring. To demonstrate this, we count the number of possible conformations of the ring for a given opening angle taking steric constraints into account. We then extract the free energy from this permutation data and plot it alongside the experiments and simulations in Fig. 2. The good agreement clearly confirms that these preferences purely arise from steric constraints: there are simply fewer possible configurations that include large values of the opening angles. Indeed, for $n = 4$ –7 compact structures of the ring are required to observe the largest opening angles, as depicted in Fig. 2(a), with concomitantly fewer possible conformations of the rings. In fact these steric constraints defined the maximum of the opening angles in the first place. Comparing the difference between the minimum and maximum values of the free energy between different ring sizes we see that the difference increases with n until $n = 7$. This implies that the ratio between the observable configurations for one angle in the maximum angle range and those for any other value of the opening angle decreases. For $n = 8$, the steric constraint is partially lifted and more conformations are possible for one internal angle at the maximum possible value. As a consequence, the maximum free energy difference lowers again compared to $n = 7$.

B. Gyration radii of rings and chains

Whilst the opening angles between particles in a chain can be used to uniquely describe its conformation, they are not a very intuitive measure for how compact or extended the structure is. A better means that is also used to quantify the extent of polymer chains and colloidal bead-chains is the radius of gyration R_g , which is defined as

$$R_g = \left[\frac{1}{n} \sum_{i=1}^n |\mathbf{r}_i - \mathbf{r}_{\text{c.m.}}|^2 \right]^{1/2}, \quad (8)$$

where \mathbf{r}_i is the position of the i th sphere and $\mathbf{r}_{\text{c.m.}}$ is the position of the center of mass of the loop.

The radius of gyration of rings is expected to follow the same scaling as the radius of gyration of chains [4,38], given by [39]

$$R_g = abn^\nu, \quad (9)$$

with a a positive constant, b is the Kuhn length (approximately equal to the bond length [22]) and the Flory exponent $\nu = 3/(d+2) = 3/4$ for a self-avoiding walk in $d = 2$ dimensions [40,41]. As shown in Fig. 3(a), we find an excellent agreement between the predicted scaling law and the experimental and simulated data. The fitted value of $\nu = 0.771 \pm 0.003$ is in close agreement with the theoretically expected value from renormalization theory [40,41] of $3/4$. While we fit our data for small n over a limited range of n only, we still find the theoretically predicted scaling laws are followed despite them having been derived in the limit of large n . This scaling coefficient also agrees with the value we have previously determined for chains of $\nu = 0.726 \pm 0.005$ [22], as would be expected since the scaling coefficient should be independent of topology.

For the scaling constant a , however, we find a lower value for the rings ($a_{\text{ring}} = 0.241 \pm 0.001$) compared to the chains [22] ($a_{\text{chain}} = 0.349 \pm 0.002$). This means that, as intuitively expected, the rings are on average more compact than chains of the same number of particles. We explore the ratio between R_g^2 of the rings and chains $G = R_{g,\text{ring}}^2/R_{g,\text{chain}}^2$ in greater detail in Fig. 3(b), by comparing the simulated and experimental values to the predicted ratio of $G = 0.568$ based on renormalization theory [4,37], which is close to the values that we obtain here. Because the chain data is only available for $n = 3$ to 6 while for the loops, we consider sizes of $n = 4$ to 8, we have also determined G by dividing a_{ring}^2 by a_{chain}^2 . As shown in Fig. 3(b), the value that we obtain from the fitted scaling relations ($G = 0.48$) is also close to the theoretically expected value. Taken together, these results show that our colloidal model system exhibits the same scaling of R_g as molecular polymers based on predictions from polymer theory, which is surprising considering their low number of segments n .

Finally, in Fig. 3(c), we show the free energy of the rings in terms of their radius of gyration, which we normalized by the average value. First, we note that the agreement between the simulated and experimental data is good for all ring sizes, although we systematically observe higher free energy values at a given value of the normalized radius of gyration for experiments compared to simulations. This difference is most clearly visible at higher values of free energy and might be due to limited experimental data, as the free energy is calculated from a probability density function. Second, it becomes apparent that the distribution of the free energy in terms of the scaled radius of gyration is asymmetric for all ring sizes and that it covers a greater range for the larger ring sizes. This last observation can be intuitively understood to be caused by the increasing number of particles and also, the increasing number of degrees of freedom. Furthermore, we observe that either very compact or very extended structures are less likely than intermediate structures, with differences in the free energy of the most likely extents compared to the least likely ones reaching up to around $10 k_B T$. These differences in the free energy are likely caused by excluded volume interactions in the case of the compact structures and steric constraints to preserve the ring topology for the more extended configurations.

Another way to quantify ring configurations is to look at the mean total curvature, which is the average of the sum of all n opening angles θ_i for all observed configurations, defined as [42]

$$\langle \text{curv} \rangle = \left\langle \sum_{i=1}^n \theta_i \right\rangle_t, \quad (10)$$

where $\langle \dots \rangle_t$ denotes the average over the measurement time. Colloidal rings can be described as two-dimensional, equilateral polygons for which the total curvature is equal to 2π if they are convex. This is the case for $n = 4, 5$; see Fig. 2(a). For $n \geq 6$, concave configurations are possible and their relative number increases with colloidal ring length. Therefore, the total curvature increases with n as is shown in Fig. 2(g).

To summarize, the size of the colloidal rings can be characterized by their radius of gyration, which follows the scaling relations that are predicted from polymer theory. The ring

topology and excluded volume interactions play an important role, which may also affect the diffusive properties of the colloidal rings, which we will now consider.

C. Diffusion of flexible tetramer loops

The continuous change of the ring's configuration might also affect its short-time diffusive behavior. We will here analyze the diffusive behavior of the simplest ring shape, the tetramer, because of its simplicity and equal probability of all configurations. In Fig. 4(a), we schematically show the coordinate system relative to the center of mass (c.m.) of the tetramer loop, which is defined in Sec. II D. The position of the c.m. as function of time for a 10 min experimental measurement is depicted in Fig. 4(b). The variations in color, which indicate the instantaneous value of one of the opening angles θ , clearly show that indeed, the tetramer loops continuously change their shape while they diffuse.

These continuous shape changes could affect the translational diffusivity of the tetramer loops. However, as shown in Fig. 4(c) for the shape-dependent, short-time translational diffusivity with respect to the x and y axes, which is defined in Sec. II D, we find that the translational diffusivity is constant and does not depend on the opening angle θ . This may be explained by the fact that for tetramer loops, the radius of gyration, which is a measure for their size, is constant as well. Therefore, the translational diffusivity can be well described in terms of the average diffusivity D_T of the x and y axes that is shown in Fig. 4(d). In Figs. 4(c) and 4(d), the experimental translational diffusivity is greater than the simulated translational diffusivity, while the experimental data shows slightly larger fluctuations because of the experimental uncertainties. We have observed this difference before for flexible colloidal chains and it can likely be ascribed to the fact that in experiments, the substrate is a hydrogel with a finite slip length, while the simulations assume a no-slip boundary condition [22].

Next, we consider the rotational diffusivity of the loops, which is defined as the in-plane rotation of the x axis shown in Fig. 4(a) or, equivalently, rotation of the cluster around the out of plane axis, for a plane parallel to the substrate. From Fig. 4(e), we see that the experimentally measured rotational diffusivity is slightly lower than the simulated rotational diffusivity, but both show the same dependence on shape. Specifically, the more compact square configuration has a higher rotational diffusivity than the more extended diamond structure, as can be expected based on the greater projected surface area of the diamond structure.

Finally, from Fig. 4(f), we conclude that also the flexibility of the tetramer loop depends on its shape, although more weakly: the flexibility is somewhat larger for square configurations than for diamond configurations. This indicates that more open structures have a higher flexibility, as we have also observed for chains [21,22]. For chains of CSLBs, we have found that the experimental flexibility is 75–80% of the flexibility of the simulated chains, which is probably caused by friction of the DNA linker patch not taken into account in the simulations [22]. For the tetramer loops, however, we observe a drastically lower flexibility, namely, the experimental flexibility is just $(20 \pm 4)\%$ of the simulated one, as shown

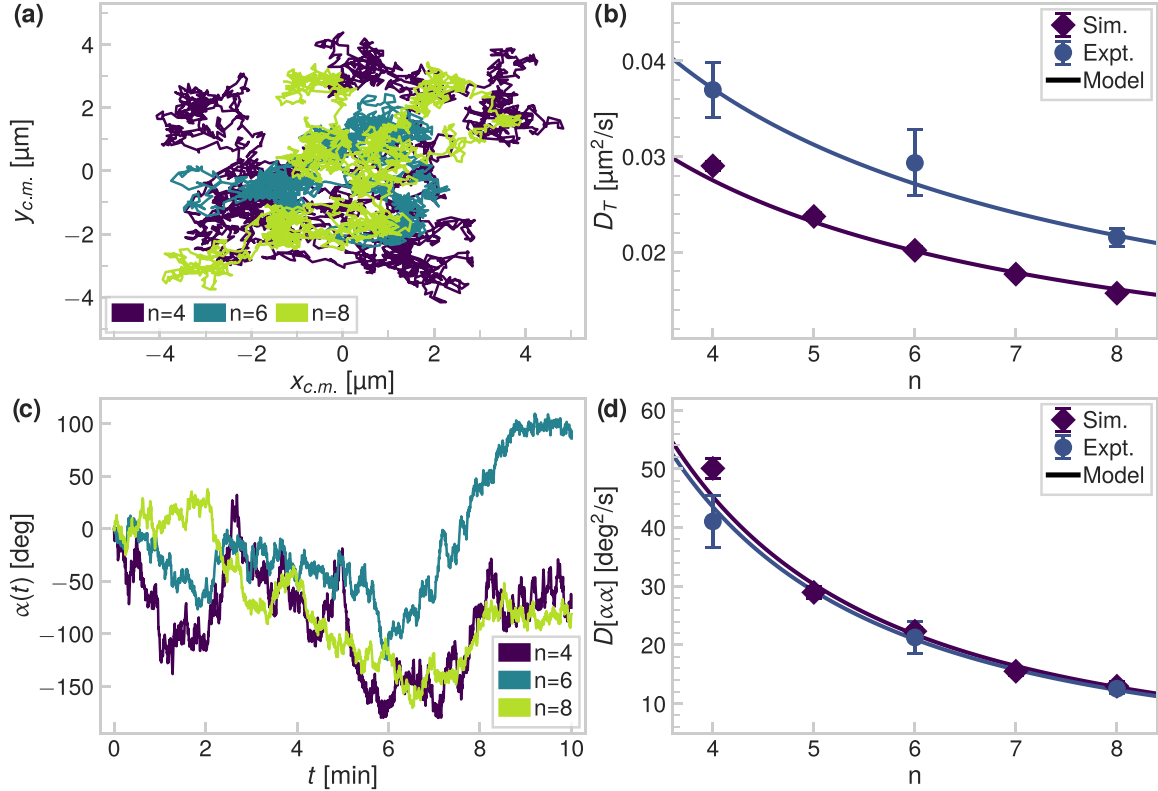


FIG. 5. Shape-averaged translational and rotational short-time diffusivity. (a) The position of the center of mass of three experimental 10 min measurements of a tetramer, hexamer and octamer ring. (b) Translational diffusivity of the rings as function of ring size n . The experimental diffusivity is greater than for the simulated data, both follow the same scaling described by Eq. (11). (c) The orientation α with respect to the initial orientation of three experimental rings as function of time. (d) The rotational diffusivity of rings as function of n shows the same behavior for the experimental and simulated data, which can be described by Eq. (12).

in Fig. 4(f). This indicates that the tetramer loops experience more interparticle friction compared to the tetramer chains. Indeed, there is one extra bond in the tetramer rings compared to the tetramer chains, which will not only lead to an increase in interparticle friction, but also imposes an additional constraint. We will discuss this difference in more detail in the next section.

D. Shape-averaged diffusivity of rings and chains

1. Translational and rotational diffusivity

Having characterized the diffusivity of the tetramer loops, it is interesting to determine how the diffusivity scales with loop size n . A detailed shape-dependent study of the diffusivity is not feasible due to the fast increase in degrees of freedom with n , and hence we instead consider the shape-averaged, short-time diffusivity of the colloidal rings. In Fig. 5(a), we show the center of mass (c.m.) position for a tetramer, hexamer and octamer loop, as tracked from 10 min experimental measurements. From this, we extract the short-time translational diffusivity D_T , which is defined in Sec. II D, as function of ring size n , see Fig. 5(b). We note that the experimental diffusivity is slightly larger than in the simulations, as we had observed previously for the tetramer loops and the flexible chains [22], probably due to the different boundary conditions in experiments and simulations. We hypothesize this is due to the no-slip boundary condition on the substrate that is used

in the simulations, while in the experiments the substrate is a hydrogel that has a finite slip length.

Second, the translational diffusivity of rings decreases as function of their size, as is expected, which we have previously shown for flexible chains [22]. In fact, based on Kirkwood-Riseman theory [43], the translational diffusivity D_T of both chains and loops are expected to scale as

$$D_T \propto 1/R_g \propto n^{-\nu}, \quad (11)$$

where the radius of gyration R_g is defined in Eq. (9). By fitting the simulated data in Fig. 5 using Eq. (11), we indeed find great agreement between model and data for $\nu = 0.771 \pm 0.003$, the value we have found in Sec. III B. Deviations from the model are slightly greater in the experimental data of the colloidal rings. Nonetheless, both the experimental and simulated data are in agreement with the expected Kirkwood-Riseman scaling.

Comparison of the exponent ν we have found with measurements on the 2D diffusion of cyclic polymers is intrinsically difficult, because for the polymers, such an experiment requires adsorption of the molecules to an interface. The presence of surface asperities hinders free diffusion of cyclic polymers on the surface due to their ringlike topology and leads to a Rouse scaling law. In this case, the translational diffusion coefficient relates to the molecular weight, $M_n \propto n$, as $D_T \propto M_n^{-\mu}$, where μ was found to be $\mu = 0.75$ for short ($n < 70$) cyclic polymers and $\mu = 1$ for long cyclic polymers

[44]. Experiments on high M_w cyclic polystyrene molecules in a good solvent and adsorbed to silica quartz confirmed $\mu = 1.00 \pm 0.10$ [10]. In our colloidal model system, adhesion to the surface is not necessary because gravity provides a quasi-2D confinement. Still, we find $\nu = 0.771 \pm 0.003$ close to the value for μ .

While the diffusivity of both rings and chains exhibits the same scaling, the ratio of their diffusion coefficients is predicted to be greater than unity, and independent of n . For long polymers, the ring-to-chain diffusivity ratio $K \equiv D_{T,\text{ring}}/D_{T,\text{chain}}$ is predicted to be approximately equal to $K = 3\pi/8 \approx 1.2$ based on Kirkwood-Riseman theory [37,45]. Renormalization group calculations predicted $K = e^{3/8} = 1.45$ [46]. Reported experimental values for synthetic polymer solutions vary between $K = 1.11$ – 1.2 [47–49] and $K = 1.36$ [50]; for short plasmid DNA $K = 1.24$ [51] and for longer single DNA molecules $K = 1.32$ was found [9]. To obtain the ratio K based on our data, we calculate the ratio of the model fits for chains and rings for $n = 4$ – 8 . For the simulated data, we find that on average $K = 1.04 \pm 0.01$, whereas the experimental data yields $K = 1.08 \pm 0.01$. These values are close to the predicted ratio based on Kirkwood-Riseman theory and similar to measurements on synthetic polymer solutions. As expected, the rings show a slightly greater diffusivity, which is explained by their smaller radius of gyration compared to chains of the same number of particles.

In the same fashion as for the translational diffusivity, we can determine the shape-averaged, short-time rotational diffusivity by calculating a rotation angle as function of time. Here, we calculate the angle α from the rotation of the \hat{x} vector defined by Eq. (2) with respect to x axis of the laboratory frame, as depicted schematically in Fig. 4(a) for the tetramer loop. Figure 5(c) shows how this rotation angle α changes as function of time for three experimental measurements of a tetramer, hexamer, and octamer loop. Based on the mean-squared angular displacements of α , the rotational diffusivity can be calculated in turn.

The rotational diffusivity is shown in Fig. 5(d), from which it can be seen that the experimental values are very close to the simulated ones. Analogous to the translational diffusivity, the rotational diffusivity follows the same scaling as for chainlike objects, given by [43]

$$D[\alpha\alpha] \propto \frac{\ln(2L/b)}{L^3}, \quad (12)$$

where b is the Kuhn length (approximately equal to the bond length) and $L = b[1 + (n-1)^\nu]$, with n the number of particles and ν the Flory exponent. Indeed, in Fig. 5(e) we find a good fit of the experimental and simulated data using Eq. (12) for $\nu = 0.771 \pm 0.003$, the value we have found in Sec. III B.

Last, we compare the ratio of rotational diffusivities of rings and chains for the available data of chains [22] and rings. We use a method analogous to the determination of K , the ratio of translational diffusivities, and calculate the ring-to-chain rotational diffusivity ratio $K_r \equiv D[\alpha\alpha]_{\text{ring}}/D[\alpha\alpha]_{\text{chain}}$. For the simulated data, we find that on average $K_r = 2.18 \pm 0.10$, whereas the experimental data yields $K_r = 1.86 \pm 0.01$.

In summary, the smaller average radius of gyration of flexible rings compared to chains of the same number of particles has implications for both their translational and rotational

diffusivity. For both diffusion constants, the rings have a higher diffusivity as expected and this effect is most pronounced for rotational diffusion, where rings exhibit a rotational diffusion that is approximately twice as high as that of chains. The ratio that we find for the translational diffusion of rings and chains is close to the theoretically expected value of approximately 1.2 based on Kirkwood-Riseman theory [37,45]. Therefore, the Kirkwood-Riseman model is found to be an excellent model for predicting the shape-averaged short-time diffusivities of flexible colloidal rings and chains.

2. Flexibility or conformational diffusion

Besides translation and rotation, flexible colloidal objects feature another diffusion coefficient stemming from changes in their conformation [52,53]. For rings of size n the number of conformational degrees of freedom is given by $n-3$ based on Maxwell counting [54]. It is therefore not feasible to characterize the displacements in terms of the initial shape for larger values of n as we have done previously for chains with three and four segments [21,22]. Instead, we calculate the shape-averaged probability distributions of $\Delta\theta$ for all ring sizes from the simulated data [see Fig. 6(a)]. As the ring size n increases, the distribution becomes slightly broader. This is expected, because the confinement of the motion by the constraint imposed by the ring closure condition is reduced, the larger the ring becomes. We characterize this broadening by measuring the standard deviation σ_n of the distribution, whose nonlinear dependence with n is shown in the inset.

From the angular displacements of the flexible loops, we can determine their conformational diffusivity $D[\theta\theta]$, or flexibility, from the slope of the mean-squared angular displacement as given by Eq. (6). This is an analogous definition of a diffusion constant in terms of bond angles instead of bead positions. From Fig. 6(b), we can observe that for both the simulated and experimental data, the flexibility indeed increases as function of loop size n , as we had expected based on Fig. 6(a). The experimental flexibility is lower than the simulated one, which is likely caused by interparticle friction stemming from the DNA linker patch between the particles. This friction is not modeled in the simulations and therefore the simulated flexibility is higher, as we had observed previously for colloidal chains [22].

The conformational diffusion coefficient $D_n[\theta\theta]$ shows a nonlinear dependence with increasing ring size. This can be understood from the fact that the standard deviation σ_n and $D_n[\theta\theta]$ are related through $D_n[\theta\theta] = \sigma_n^2/(2n\tau)$ [see also Eq. (6)]. While these data have been averaged over all internal opening angles, averaging is not the cause for the nonlinear behavior, as we find the same behavior for the conformational diffusion coefficient of a single opening angle in the ring.

Interestingly, the chain length above which $D_n[\theta\theta]$ starts to saturate coincides with the chain length above which the steric constraints in the opening angle are lifted, and the free energy differences between small and large opening angles decrease again; see Fig. 2. At the same time, the number of conformational degrees of freedom increases and the distribution of the radius of gyration broadens. Combined, this leads to a greater range of possible displacements that are sterically allowed and

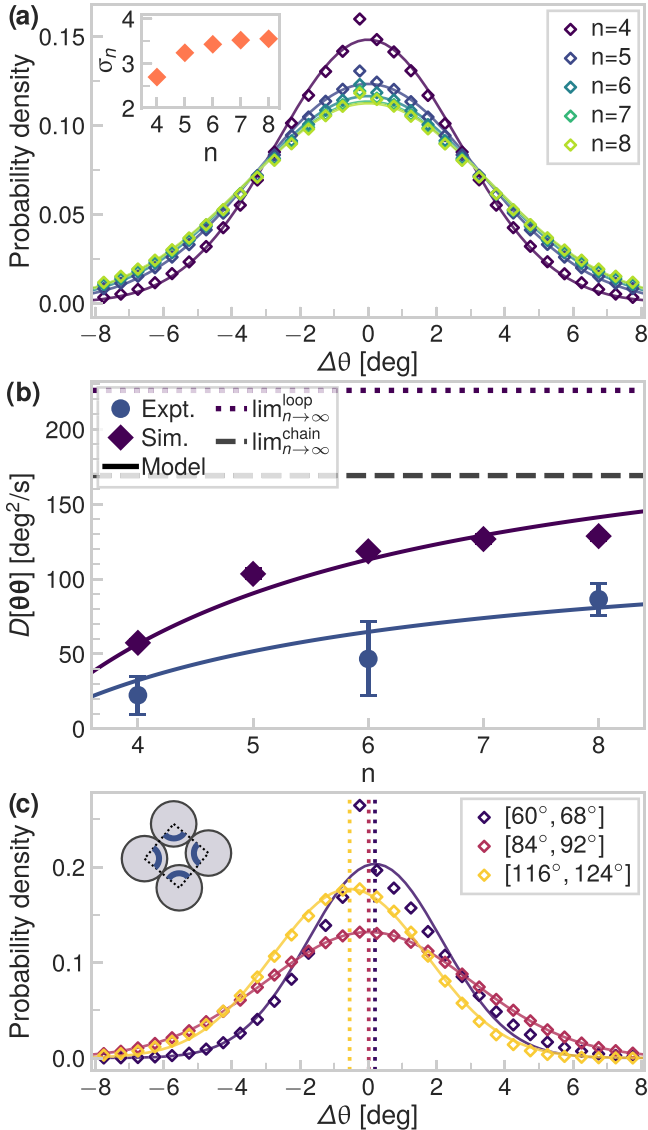


FIG. 6. Shape-averaged flexibility. (a) Probability density of the angular displacements $\Delta\theta$ of all loops (simulated data) averaged over all opening angles θ . Solid lines show a fit of a Gaussian. The inset shows the standard deviation σ_n of $\Delta\theta$ vs n . (b) Flexibility of the rings as function of n . Solid lines are fits of Eq. (15). Dotted lines show the expected flexibility of chains and loops for $n \rightarrow \infty$. (c) Probability density of the angular displacements $\Delta\theta$ of the tetramer loops (simulated data), binned per opening angle θ (see legend). Dotted lines show the mean angular displacement, solid lines show a fit of a Gaussian.

therefore, a broader probability distribution for the larger ring sizes.

We therefore hypothesize that the constraints stemming from the requirement that the structures need to remain a closed ring are causing this dependence on n . This ring constraint imposes that all displacements $\Delta\theta_i$ of the internal opening angles add up to zero between two time steps that are a lag time τ apart. More importantly, the $n - 3$ conformational degrees of freedom require that only $n - 3$ of these displacements can be chosen independently. The remaining

three displacements are then determined by the requirement of the closed ring topology. If we consider the independent displacements to have a distribution with standard deviation $\sigma_{\text{indep.}}$, and the dependent displacements to have a distribution with standard deviation $\sigma_{\text{dep.}}$, we can write

$$\sigma_n^2 = (n - 3)\sigma_{\text{indep.}}^2 + 3\sigma_{\text{dep.}}^2. \quad (13)$$

However, as the three dependent displacements are completely determined by the choice of the independent displacements, their distribution has an effective standard deviation $\sigma_{\text{dep.}} = 0$. Thus,

$$\sigma_n^2 = (n - 3)\sigma_{\text{indep.}}^2, \quad (14)$$

and we find that

$$D_n[\theta\theta] = \frac{(n - 3)\sigma_{\text{indep.}}^2}{2n\tau}. \quad (15)$$

By fitting this prediction to our experimental data, we find $\sigma_{\text{indep.}}^2/(2\tau) = (129 \pm 16) \text{ deg}^2/\text{s}$ and for the simulated data we find $\sigma_{\text{indep.}}^2/(2\tau) = (226 \pm 4) \text{ deg}^2/\text{s}$ [indicated by the dotted line in Fig. 6(b)], which is the value that the flexibility saturates at for large n . It should be noted that this is a prediction derived from small n data and does not take any additional large n effects into account. Based on the derived scaling, the flexibility is expected to saturate at large n , but this remains to be tested in future work. The ratio between the experimental and simulated flexibility is 0.57 ± 0.07 . This ratio is close to the value of 0.75 to 0.8 that we had found previously for colloidal chains [22]. This suggests that the decrease in experimental flexibility is approximately the same for chains and loops. Most likely, it is caused by friction that is not accounted for in the simulations.

Our description of the flexibility of colloidal loops in Eq. (15) predicts that for large n , the flexibility should approach a limiting value of $\sigma_{\text{indep.}}^2/(2\tau)$. Interestingly, for large ring sizes, the flexibility does not depend on n anymore, just as the flexibility of colloidal chains is independent of the chain size. Therefore, it is instructive to compare the values of $\sigma_{\text{indep.}}^2/(2\tau)$ that we have found for colloidal rings to those we had determined previously for colloidal chains. For chains, we have found an average flexibility of $(168 \pm 4) \text{ deg}^2/\text{s}$ [indicated by the dashed line in Fig. 6(b)] for our simulated data and $(100 \pm 20) \text{ deg}^2/\text{s}$ for the experimental data [22]. Therefore, we find that the ratio between the flexibility of loops and chains is 1.34 ± 0.03 for the simulated data and 1.30 ± 0.30 for the experimental data. These values agree within error. They indicate that for large n , the flexibility of colloidal loops is greater than that of colloidal chains.

A possible explanation for the prediction that colloidal loops have a greater conformational flexibility than colloidal chains for $n \geq 8$ might be found in the differences of their translational diffusivity. For ring-structures, the translational diffusivity is larger by a factor K of 1.1 to 1.4, as discussed in Sec. III D. Indeed, the ratio between the flexibility of loops and chains that we find here also falls into this range of values for K . Therefore, it is likely that the larger flexibility of the colloidal rings for $n \geq 8$ is a result of their greater translational diffusivity compared to colloidal chains of the same size. We note that the translational diffusivity has also

previously been identified to be important for the flexibility, where it was found that the maximum value of the flexibility was determined by the translational diffusion coefficient of the individual spheres [22,55].

Finally, we also consider effects that stem from excluded volume interactions and hydrodynamics. To do so we consider the simplest ring that has just a single degree of freedom, the tetramer loop. In Fig. 6(c) we show the probability density function of displacements $\Delta\theta$ during a lag time of $\tau = 0.05$ s for the simulated data for three initial configurations. First, for the square configuration ($\theta \in [84^\circ, 92^\circ]$), we find that as expected displacements are symmetrically distributed around zero. This is in contrast to the diamond configurations: for $\theta \in [60^\circ, 68^\circ]$ we find a small bias toward positive displacements and for $\theta \in [116^\circ, 124^\circ]$ we find the opposite, a bias toward negative displacements. The origin of these shifts likely stems from a combination of the constraint that the internal opening angle cannot be smaller than 60° or larger than 120° , and hydrodynamic interactions when particles that span the internal opening angle are close to each other [21].

In addition to the mean value, the distribution for square configurations is also broader than the distribution of the diamond configurations. This leads to the slightly larger diffusivity for the square configurations that we have observed in Fig. 4(f) for the short-time diffusivity of tetramer loops. Therefore, we hypothesize that the differences in flexibility as function of angle θ that we have observed in Fig. 4(f) are in part caused by steric constraints. Other contributions stem from hydrodynamic interactions between the particles.

To summarize, we have found that the flexibility of the colloidal loops increases as function of loop size n . For $n \geq 8$, the flexibility saturates to a higher value than the flexibility of colloidal chains. For smaller loop sizes, steric restrictions lead to a lower flexibility. We have proposed a scaling relation in terms of the number of conformational degrees of freedom and find that it describes our simulated and experimental data well. The observed scaling could have implications for other microscopic ringlike structures found in biology, such as ring polymers. Additionally, the observation that in addition to hydrodynamic properties, steric constraints can have a large effect on the conformational diffusivity of flexible objects as well could have broader implications beyond ringlike structures.

IV. CONCLUSIONS

In conclusion, we have studied a model system of flexible colloidal loops using experiments and simulations, to gain greater insight in the physical processes that govern the

behavior of reconfigurable ringlike microscopic objects, such as ring polymers. First, we have found that for the loops consisting of four to eight spheres, steric constraints have a large effect on the possible conformations of the rings, as characterized by their opening angles and radius of gyration. Indeed, we have found differences in free energy of around $6 k_B T$ between the most and least likely configurations of the rings. We found that the scaling of the radius of gyration scales according to Flory theory, and that the ratio of radii of gyration of rings and chains is close to the expected value derived for molecular polymers by renormalization theory.

The diffusive properties of the rings show the same scaling as function of size as flexible colloidal chains and follows predictions based on Kirkwood-Riseman theory. We find that the ratio between the translational diffusivity of rings and chains is close to the expected theoretical value and observe that the rotational diffusivity of rings is approximately twice as high as that of chains. In contrast to chains, for which the flexibility is nearly constant, the flexibility, or conformational diffusivity, of rings increases as function of ring size up to a limiting value, set by hydrodynamic friction. We propose a simple scaling that considers the number of conformational degrees of freedom in the displacements and found that the proposed scaling is in good agreement with the experimental and simulated data.

This observed scaling could have broader implications for other microscopic ringlike structures found in synthetic and biological systems, such as ring polymers. In particular, our observation that topological constraints can have a large effect on the conformational diffusivity of flexible objects as well could have broader implications beyond ringlike structures. Therefore, it would be interesting to investigate the conformational diffusivity of (model systems for) structures where geometric constraints play a significant role, such as in floppy colloidal crystals and intrinsically disordered proteins.

ACKNOWLEDGMENTS

We thank Ali Azadbakht for the design and setup of the Optical Tweezers and his technical support. We are grateful to Aleksandar Donev and Brennan Sprinkle for fruitful discussions and for providing us with example code for the simulations. We thank Yair Shokef and Martin van Hecke for useful discussions. The simulations were partly performed using the ALICE compute resources provided by Leiden University. This project has received funding from the European Research Council (ERC) under the European Union's Horizon 2020 research and innovation program (Grant Agreement No. 758383).

-
- [1] T. McLeish, Polymers without beginning or end, *Science* **297**, 2005 (2002).
 - [2] J. D. Halverson, W. B. Lee, G. S. Grest, A. Y. Grosberg, and K. Kremer, Molecular dynamics simulation study of nonconcatenated ring polymers in a melt. II. Dynamics, *J. Chem. Phys.* **134**, 204905 (2011).
 - [3] D. Michieletto and M. S. Turner, A topologically driven glass in ring polymers, *Proc. Natl. Acad. Sci. USA* **113**, 5195 (2016).
 - [4] J. Prentis, Spatial correlations in a self-repelling ring polymer, *J. Chem. Phys.* **76**, 1574 (1982).
 - [5] B. W. Soh, A. R. Klotz, R. M. Robertson-Anderson, and P. S. Doyle, Long-Lived Self-Entanglements in Ring Polymers, *Phys. Rev. Lett.* **123**, 048002 (2019).
 - [6] J. D. Halverson, J. Smrek, K. Kremer, and A. Y. Grosberg, From a melt of rings to chromosome territories: The role of

- topological constraints in genome folding, *Rep. Prog. Phys.* **77**, 022601 (2014).
- [7] S. Liu, S. Murata, and I. Kawamata, DNA ring motif with flexible joints, *Micromachines* **11**, 987 (2020).
- [8] M. F. Serag, M. Abadi, and S. Habuchi, Single-molecule diffusion and conformational dynamics by spatial integration of temporal fluctuations, *Nat. Commun.* **5**, 5123 (2014).
- [9] R. M. Robertson, S. Laib, and D. E. Smith, Diffusion of isolated DNA molecules: Dependence on length and topology, *Proc. Natl. Acad. Sci. USA* **103**, 7310 (2006).
- [10] S. Ye, Q. Tang, J. Yang, K. Zhang, and J. Zhao, Interfacial diffusion of a single cyclic polymer chain, *Soft Matter* **12**, 9520 (2016).
- [11] R. M. Robertson and D. E. Smith, Strong effects of molecular topology on diffusion of entangled DNA molecules, *Proc. Natl. Acad. Sci. USA* **104**, 4824 (2007).
- [12] D. Richter, S. Gooßen, and A. Wischniewski, Topology matters: Structure and dynamics of ring polymers, *Soft Matter* **11**, 8535 (2015).
- [13] F. M. Haque and S. M. Grayson, The synthesis, properties, and potential applications of cyclic polymers, *Nat. Chem.* **12**, 433 (2020).
- [14] S. Habuchi, N. Satoh, T. Yamamoto, Y. Tezuka, and M. Vacha, Multimode diffusion of ring polymer molecules revealed by a single-molecule study, *Angew. Chem., Int. Ed.* **49**, 1418 (2010).
- [15] A. Einstein, Über die von der molekularkinetischen Theorie der Wärme geforderte Bewegung von in ruhenden Flüssigkeiten suspendierten Teilchen, *Annalen der Physik* **322**, 549 (1905).
- [16] W. Sutherland, A dynamical theory of diffusion for nonelectrolytes and the molecular mass of albumin, *London Edinburgh Dublin Philos. Mag. J. Sci.* **9**, 781 (1905).
- [17] J. Perrin, Mouvement brownien et réalité moléculaire., *Ann. Chim. Phys.* **18**, 104 (1909).
- [18] P. Swinkels, S. Stuij, Z. Gong, H. Jonas, N. Ruffino, B. van der Linden, P. Bolhuis, S. Sacanna, S. Woutersen, and P. Schall, Revealing pseudorotation and ring-opening reactions in colloidal organic molecules, *Nat. Commun.* **12**, 2810 (2021).
- [19] S. A. van der Meulen and M. E. Leunissen, Solid colloids with surface-mobile DNA linkers, *J. Am. Chem. Soc.* **135**, 15129 (2013).
- [20] M. Rinaldin, R. W. Verweij, I. Chakraborty, and D. J. Kraft, Colloid supported lipid bilayers for self-assembly, *Soft Matter* **15**, 1345 (2019).
- [21] R. W. Verweij, P. G. Moerman, N. E. G. Ligthart, L. P. P. Huijnen, J. Groenewold, W. K. Kegel, A. van Blaaderen, and D. J. Kraft, Flexibility-induced effects in the Brownian motion of colloidal trimers, *Phys. Rev. Res.* **2**, 033136 (2020).
- [22] R. W. Verweij, P. G. Moerman, L. P. Huijnen, N. E. Ligthart, I. Chakraborty, J. Groenewold, W. K. Kegel, A. van Blaaderen, and D. J. Kraft, Conformations and diffusion of flexibly linked colloidal chains, *J. Phys.: Mater.* **4**, 035002 (2021).
- [23] D. B. Allan, T. Caswell, N. C. Keim, C. M. van der Wel *et al.*, *Soft-matter/trackpy Trackpy v0.4.2*, Zenodo (2019), <https://doi.org/10.5281/zenodo.3492186>.
- [24] S. Barkley, T. G. Dimiduk, J. Fung, D. M. Kaz, V. N. Manoharan, R. McGorty, R. W. Perry, and A. Wang, Holographic microscopy with Python and HoloPy, *Comput. Sci. Eng.* **22**, 72 (2020).
- [25] B. Sprinkle, E. B. van der Wee, Y. Luo, M. M. Driscoll, and A. Donev, Driven dynamics in dense suspensions of microrollers, *Soft Matter* **16**, 7982 (2020).
- [26] S. Delong, F. Balboa, B. Delmotte, B. Sprinkle, A. Donev *et al.*, *stochasticHydroTools/RigidMultiblobsWall: Rigid Multiblobs in half-space (v. 427d241)* (2020), <https://github.com/stochasticHydroTools/RigidMultiblobsWall>.
- [27] J. W. Swan and J. F. Brady, Simulation of hydrodynamically interacting particles near a no-slip boundary, *Phys. Fluids* **19**, 113306 (2007).
- [28] J. Rotne and S. Prager, Variational treatment of hydrodynamic interaction in polymers, *J. Chem. Phys.* **50**, 4831 (1969).
- [29] H. Yamakawa, Transport properties of polymer chains in dilute solution: Hydrodynamic interaction, *J. Chem. Phys.* **53**, 436 (1970).
- [30] E. Wajnryb, K. A. Mizerski, P. J. Zuk, and P. Szymczak, Generalization of the Rotne-Prager-Yamakawa mobility and shear disturbance tensors, *J. Fluid Mech.* **731**, R3 (2013).
- [31] F. Balboa Usabiaga, B. Delmotte, and A. Donev, Brownian dynamics of confined suspensions of active microrollers, *J. Chem. Phys.* **146**, 134104 (2017).
- [32] W. A. Wegener, Center of diffusion of flexible macromolecules, *Macromolecules* **18**, 2522 (1985).
- [33] B. Cichocki, M. Rubin, A. Niedzwiecka, and P. Szymczak, Diffusion coefficients of elastic macromolecules, *J. Fluid Mech.* **878**, R3 (2019).
- [34] X. Michalet, Mean-square displacement analysis of single-particle trajectories with localization error: Brownian motion in an isotropic medium, *Phys. Rev. E* **82**, 041914 (2010).
- [35] I. Chakraborty, V. Meester, C. Van Der Wel, and D. J. Kraft, Colloidal joints with designed motion range and tunable joint flexibility, *Nanoscale* **9**, 7814 (2017).
- [36] See Supplemental Material at <http://link.aps.org/supplemental/10.1103/PhysRevE.107.034602> for movies of flexible rings of size $n = 4, 6$, and 8 .
- [37] G. A. Hegde, J.-f. Chang, Y.-l. Chen, and R. Khare, Conformation and diffusion behavior of ring polymers in solution: A comparison between molecular dynamics, multiparticle collision dynamics, and lattice Boltzmann simulations, *J. Chem. Phys.* **135**, 184901 (2011).
- [38] O. Jagodzinski, E. Eisenriegler, and K. Kremer, Universal shape properties of open and closed polymer chains: Renormalization group analysis and Monte Carlo experiments, *Journal de Physique I* **2**, 2243 (1992).
- [39] P.-G. De Gennes, *Scaling Concepts in Polymer Physics* (Cornell University Press, Ithaca, NY, 1979).
- [40] R. D. Kamien, Flory exponents from a self-consistent renormalization group, *Journal de Physique I* **3**, 1663 (1993).
- [41] X. Wang and K. Wang, Calculation of the Flory exponent using the Renormalization theory, *Polym. J.* **27**, 515 (1995).
- [42] A. Y. Grosberg, Total curvature and total torsion of a freely jointed circular polymer with $n \gg 1$ segments, *Macromolecules* **41**, 4524 (2008).
- [43] J. Riseman and J. G. Kirkwood, The intrinsic viscosity, translational and rotatory diffusion constants of rod-like macromolecules in solution, *J. Chem. Phys.* **18**, 512 (1950).
- [44] D. Mukherji, G. Bartels, and M. H. Müser, Scaling Laws of Single Polymer Dynamics Near Attractive Surfaces, *Phys. Rev. Lett.* **100**, 068301 (2008).

- [45] M. Fukatsu and M. Kurata, Hydrodynamic properties of flexible-ring macromolecules, *J. Chem. Phys.* **44**, 4539 (1966).
- [46] B. Schaub and D. B. Creamer, Renormalization group study of the translational diffusion constant for a ring polymer, *Phys. Lett. A* **121**, 435 (1987).
- [47] M. Duval, P. Lutz, and C. Strazielle, Hydrodynamic dimensions of ring-shaped macromolecules in a good solvent, *Die Makromolekulare Chemie, Rapid Commun.* **6**, 71 (1985).
- [48] D. F. Hodgson and E. J. Amis, Dilute solution behavior of cyclic and linear polyelectrolytes, *J. Chem. Phys.* **95**, 7653 (1991).
- [49] J. S. Higgins, K. Ma, L. K. Nicholson, J. B. Hayter, K. Dodgson, and J. A. Semlyen, Studies of cyclic and linear poly(dimethyl siloxanes): 12. Observation of diffusion behaviour by quasielastic neutron scattering, *Polymer* **24**, 793 (1983).
- [50] P. C. Griffiths, P. Stilbs, G. E. Yu, and C. Booth, Role of molecular architecture in polymer diffusion: A PGSE-NMR study of linear and cyclic poly(ethylene oxide), *J. Phys. Chem.* **99**, 16752 (1995).
- [51] G. Voordouw, Z. Kam, N. Borochoy, and H. Eisenberg, Isolation and physical studies of the intact supercoiled: The open circular and the linear forms of ColE1-plasmid DNA, *Biophys. Chem.* **8**, 171 (1978).
- [52] W. A. Wegener, Bead models of segmentally flexible macromolecules, *J. Chem. Phys.* **76**, 6425 (1982).
- [53] S. C. Harvey, P. Mellado, and J. G. De La Torre, Hydrodynamic resistance and diffusion coefficients of segmentally flexible macromolecules with two subunits, *J. Chem. Phys.* **78**, 2081 (1983).
- [54] J. C. Maxwell, On the calculation of the equilibrium and stiffness of frames, *London Edinburgh Dublin Philos. Mag. J. Sci.* **27**, 294 (1864).
- [55] A. McMullen, M. Holmes-Cerfon, F. Sciortino, A. Y. Grosberg, and J. Brujic, Freely Jointed Polymers Made of Droplets, *Phys. Rev. Lett.* **121**, 138002 (2018).